# A novel ferroelectric nanopillar multi-level cell memory[☆],[☆☆],[★]

Hyeongu Lee, Mincheol Shin [*]

*School of Electrical Engineering, Korea Advanced Institute of Science and Technology, 291, Daehak-ro, Yuseong-gu, 34141, Daejeon, South Korea*

## ARTICLE INFO

## ABSTRACT

In this work, we present a novel multi-level non-volatile memory (NVM) device where ferroelectric (FE) nanopillars are embedded in a dielectric (DE) medium. Using our in-house 3D phase field simulator developed to treat the FE–DE composite system stably, we demonstrate that $n$ FE nanopillars can generate more than $2^n$ states, enabling high storage capacity. The multistates of the pillar array device are attributed to the depolarization field modulation with the pillar height and the multi-domain topological states of nanoscale FE structures.

## 1. Introduction

Ferroelectric (FE) materials with reversible polarization states have attracted attention for non-volatile memory (NVM) applications [1]. To increase the storage capacity of the FE-based NVM, there have been reported various device concepts to achieve multistates in a single cell. For example, the multi-layer structure of FE and dielectric (DE) layers can exhibit multistates through sequential switching of each FE layer [2] or modulating the number of switching pathways [3]. These approaches generate multistates that are fully poled FE states. In addition to using the poled states, multi-domain topological states of the nanoscale FE structures can be also utilized [4]. In this work, we present a novel multi-level NVM of FE nanopillars embedded in a DE medium. Using 3-dimensional (3-D) finite element time-dependent Ginzburg–Landau (TDGL) simulations, we show that a two-nanopillar system can create more than 4 states modulating the pillar heights.

## 2. Method

The time evolution of the polarization (**P**) is obtained by solving the TDGL equation written as

$$-\rho \frac{dP_i(\boldsymbol{r},t)}{dt} = \frac{\delta F}{\delta P_i(\boldsymbol{r},t)} \tag{1}$$

$$F = \int_V dV \, \alpha_{ij} P_i P_j + \alpha_{ijkl} P_i P_j P_k P_l \\ + \alpha_{ijklnm} P_i P_j P_k P_l P_n P_m - g_{ijkl} \partial_i P_k \partial_j P_l + P_i \nabla_i \psi \tag{2}$$

where $i, j, k, l, n, m = x, y, z$, and $\rho$ is the kinetic coefficient, $F$ is the total free energy, $g_{ijkl}$ is the gradient energy coefficient, $\alpha_{ij}, \alpha_{ijkl}, \alpha_{ijklnm}$ are the Landau bulk free energy coefficients, and $\psi$ is the electrostatic potential.

For a composite system of FE and DE, the discontinuity of **P** occurs at the interface between FE and DE. The discontinuity results in the depolarization field which plays an important role in **P** switching. In addition, it can cause numerical instability with oscillations and divergence [5]. To accurately incorporate the depolarization field effect and resolve the issue of the numerical instability, we have developed 3D finite element phase-field simulator where TDGL equation is solved together with Poisson's equation using local discontinuous Galerkin method [6]. The in-house simulator can treat 3D geometrical model $(x, y, z)$ and **P** vector $(P_x, P_y, P_z)$. In this work, however, a uniaxial ferroelectric is assumed whose **P** direction is parallel to $z$-axis. The Eq. (1) and (2) are reduced to

$$\rho \frac{\partial P_z}{\partial t} + \alpha P_z + \beta P_z^3 + \gamma P_z^5 \\ - g_{11} \partial_z^2 P_z - g_{44} \partial_x^2 P_z - g_{44} \partial_y^2 P_z + \partial_z \psi = 0 \tag{3}$$

All the simulation parameters are shown in Table 1. The landau coefficients of $\alpha$, $\beta$ and $\gamma$ are taken from [7] whose fitted parameters correspond to HZO with the thickness of 10 nm. TDGL equation in Eq. (1) is non-linear dynamic system. An Implicit time integration scheme is needed to properly solve the system. However, the implicit scheme is computationally expensive. In order to correctly and efficiently solve the system, diagonally implicit Runge–Kutta method [8].

**Table 1**
Simulation parameters. The gradient coefficients of $g_{11}$ and $g_{44}$ and the kinetic coefficient of $\rho$ are taken from [9] and [10], respectively. $\epsilon_{FE}$ and $\epsilon_{DE}$ are the relative permittivities of the ferroelectric and dielectric region, respectively.

| Parameters | Value |
|---|---|
| $\alpha$ | $-2.5 \times 10^9$ Vm/C |
| $\beta$ | $6.0 \times 10^{10}$ Vm$^5$/C$^3$ |
| $\gamma$ | $1.5 \times 10^{11}$ Vm$^9$/C$^5$ |
| $g_{11}$ | $0.5 \times 10^{-10}$ m$^3$ V/C |
| $g_{44}$ | $2.0 \times 10^{-10}$ m$^3$ V/C |
| $\rho$ | $30\ \Omega$ m |
| $\epsilon_{FE}$ | 23 |
| $\epsilon_{DE}$ | 10 |
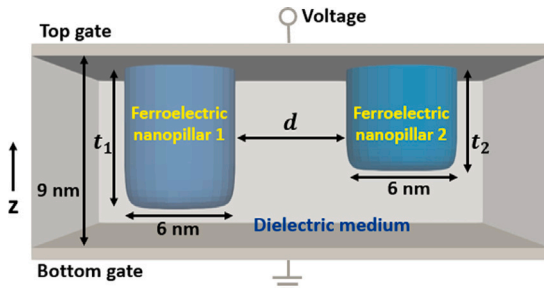


**Fig. 1.** Schematic structure of double FE nanopillar device.
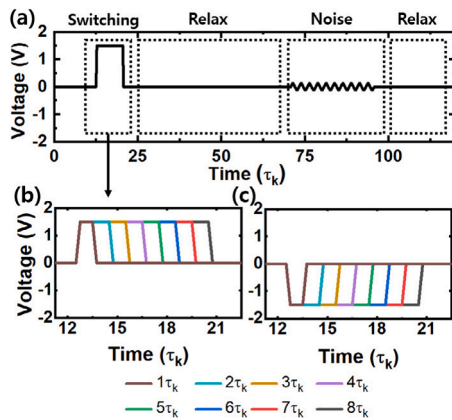


**Fig. 2.** (a) Pulse scheme and step pulse variation for (b) MDS↑ and (c) MDS↓.

## 3. Results and discussions

A schematic of FE nanopillar array structure is presented in Fig. 1. FE nanopillars with a diameter of 6 nm are embedded in the dielectric medium of $Al_2O_3$ with a thickness of 9 nm. A single FE nanopillar in the DE medium can take at least two mono domain states (MDS) where the **P** shows fully up-poled state (MDS↑) and down-poled state (MDS↓). To explore other topological states that can be accessed, the pulse scheme is designed as shown in Fig. 2(a). **P** of the single FE nanopillar was initially set to MDS↑ or MDS↓. The pulse voltage was set to 1.5 V and its width varied from $1\tau_k$ to $8\tau_k$ where $\tau_k$ is the time scale of TDGL simulation, defined as $\tau_k = \rho/(2|\alpha|)$. To check the stability of the relaxed FE states, the noise pulse of triangular pulse train with the voltage of 0.15 V and the period of $2.5\tau_k$ was applied.

Fig. 3(a) and (b) show the change of the average **P** ($P_{AVG}$) over time. Interestingly, the nanopillar shows two additional topological states besides MDS↑ and MDS↓. By the pulse width of $2\tau_k$ to $4\tau_k$, **P** near the center of MDS↑ is partially switched to opposite direction. After
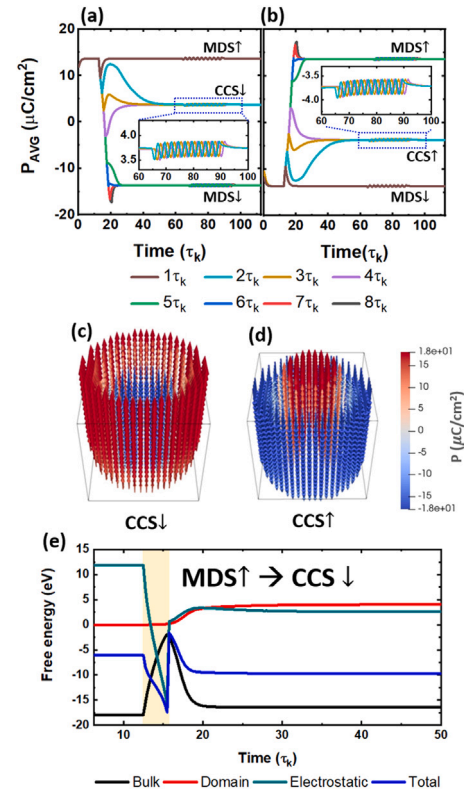


**Fig. 3.** The change of **P** over time for the initial (a) MDS↑ and (b) MDS↓. The inset shows the response of CCS to the noise pulse. The topological configuration of **P** of (c) CCS↓ ad (d) CCS↑. (e) The change of the free energy for the pulse width of $3\tau$ when MDS↑ switches to CCS↓. The shaded region indicates the step pulse duration.
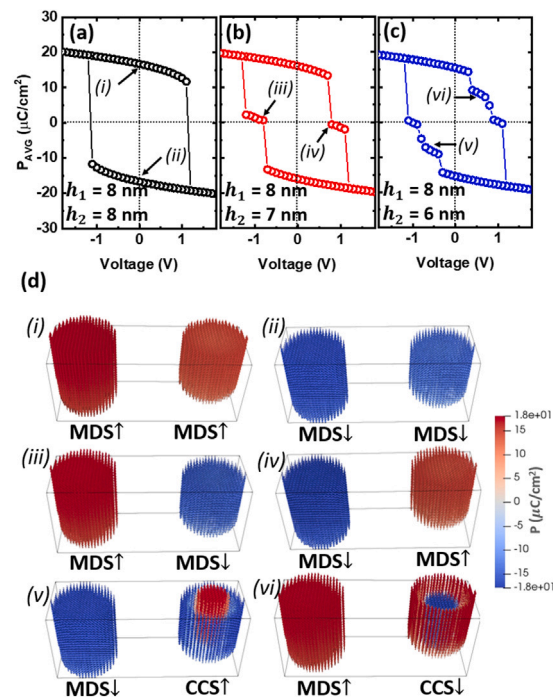


**Fig. 4.** $P_{AVG} - V_{APP}$ hysteresis loops for two FE nanopillars in dielectric medium with different pillar heights ($h_1$ and $h_2$). (a) $h_1 = h_2 = 8$ nm, (b) $h_1 = 8$ nm and $h_2 = 7$ nm, and (c) $h_1 = 8$ nm and $h_2 = 6$ nm. (d) **P** distribution of (i)-(vi) states of (a)–(c). Blue and red colors indicates the down and up **P**, respectively. (For interpretation of the references to color in this figure legend, the reader is referred to the web version of this article.)

the step pulse, **P** of the nanopillar is relaxed to cylindrical concentric state with the down-poled center (CCS↓) as illustrated in Fig. 3(c). As in the case of MDS↑, MDS↓ is switched to CCS with the up-poled center (CCS↑) in Fig. 3(d). These CCSs are induced by the Landau–Lifshitz domain branching effect where the depolarization field from the nonuniform mono domain **P** distribution reduces the polarization at the center surface [4].

The polarization configuration of the CCS results in more stable states than the MDS. Fig. 3(e) shows the change of the free energy over time for the case of the pulse width of $3\tau_k$ where MDS↑ is switched to CCS↓. After the step pulse, the domain energy increases by approximately 4.0 eV, while the electrostatic energy is significantly decreased by 9.0 eV. This gives rise to the decrease in the total energy. The CCS states remain stable even after the noise pulse is applied as shown in Fig. 3(a) and (b). It shows that the states stay in a local minimum thermodynamically and thus can be utilized for multi-level memory cell.

An array structure with $n$ FE nanopillars can have $2^n$ states, as each nanopillar has both MDS↑ and MDS↓. If the CCS can be utilized, the multiple pillar device is expected to show more than $2^n$ states. To investigate the multistate property, we simulated the devices with two FE nanopillars in the DE medium. The pillar heights ($h_1$ and $h_2$) and the inter-pillar distance ($d$) are varied to investigate the effect of the depolarization field and long-range Coulomb interaction between the nanopillars.

The simulated hysteresis loops of $P_{AVG}$ of two pillars with $h_1$ and $h_2$ as a function of the applied voltage ($V_{APP}$) are shown in Fig. 4(a)–(c). Only two states of *(i)* and *(ii)* are exhibited for the case of two identical pillars ($h_1 = h_2 = 8$ nm) in Fig. 4(a). These states result from the MDS↑ and MDS↓ of each pillar, as illustrated in panels *(i)* and *(ii)* of Fig. 4(d). **P** of the two nanopillars simultaneously switch because the depolarization fields of the two pillars are same.

The device with the two pillars shows the multi-level state if $h_1 \neq h_2$. As shown in Fig. 4, for the case of $h_1 = 8$ nm and $h_2 = 7$ nm, the two states, labeled as *(iii)* and *(iv)*, are generated besides *(i)* and *(ii)*. The two states result from the polarization switching of the shorter FE nanopillar (see panels *(iii)* and *(iv)* of Fig. 4(d)). This is because the depolarization field increases as the pillar height decreases when the total film thickness is constant, so **P** of the shorter pillar of $h_2 = 7$ nm is switched to the opposite MDS at weaker applied voltage.

It is noted that a further decrease in the pillar height of $h_2 = 6$ nm creates two additional states labeled as *(v)* and *(vi)* in Fig. 4(c). The states originate from the CCS↑ and CCS↓ of the shorter pillar as illustrated in panels *(v)* and *(vi)* of Fig. 4(d). To explore the possible hidden states which are not shown in the hysteresis loop, the step pulse simulation was conducted. In Fig. 5(a) and (b), as expected, the six states of *(i)-(iv)* can be accessed, corresponding to those in Fig. 4(d). Note that there are two hidden states of *(vii)* and *(viii)*. These states are created by CCS↑ and CCS↓ of the longer pillar, as shown in panels *(vii)* and *(viii)* of Fig. 5(c). Thus, with the two hidden states included, a total of 8 states can be accessed, which implies that a cell of the two pillars may enable 3-bit memory operation using a simple step pulse.

The long-range Coulomb interaction between the FE nanopillars affects the accessible topological states. Fig. 6(a) shows the change of $P_{AVG}$ over time for the two identical pillars for the cases of $d = 2$, 6, and 8 nm. For $d = 4$ and 6 nm, the relaxed states are identical to each other (CCS↓ and CCS↓ as illustrated in Fig. 6(b)). However, if $d$ is decreased to 2 nm, $P_{AVG}$ of the relaxed states greatly decreases by approximately 10 μC/cm², resulting in the topological configuration of two-band state (TBS) as shown in Fig. 6(b). This can be explained by the fact that the CCS↓ has up-poled **P** in the off-center region and, as $d$ decreases, the electrical repulsion between the up-poled **P** of two pillars increases. Thus, after the step pulse, MDS↑ switches to TBS rather than CCS↓.
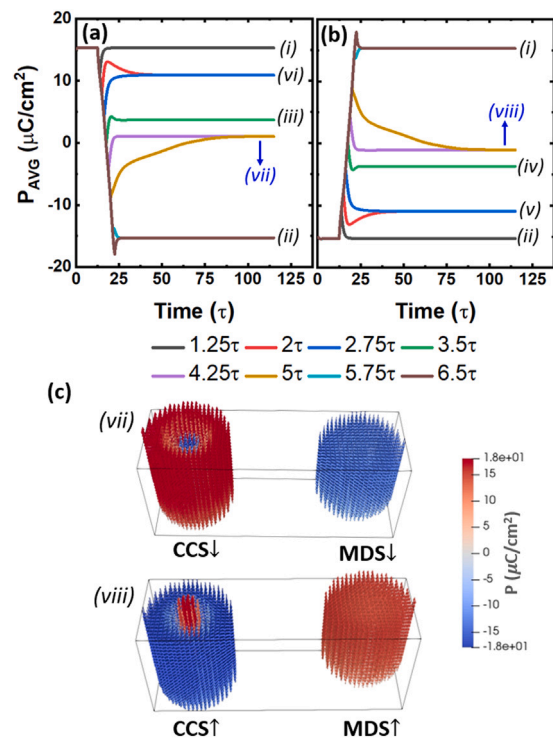


**Fig. 5.** $P_{AVG}$ as a function of time for the initial (a) MDS↑ and (b) MDS↓. (i)-(vi) states correspond to those in Fig. 4(d). (e) **P** distribution of the hidden states of (vii) and (viii).
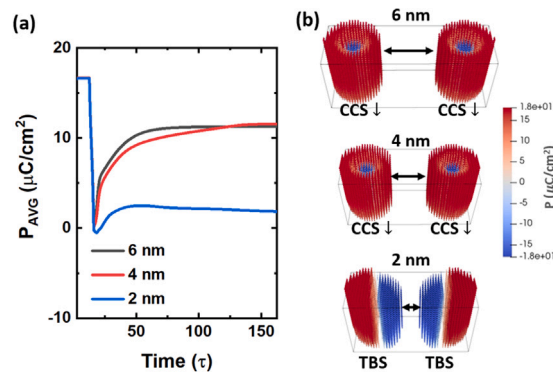


**Fig. 6.** (a) The change of $P_{AVG}$ over time for two identical FE nanopillar with heights of 8 nm and (b) the **P** distribution of the relaxed states for $d = 2$, 4, and 6 nm.

## 4. Conclusion

In this work, we propose a novel multi-level NVM using FE nanopillars in a dielectric medium. Using 3D TDGL simulations, we theoretically demonstrate that $n$ FE nanopillars can generate more than $2^n$ states. The multistates of the FE pillar system are attributed to the consecutive switching of the polarization states of the FE nanopillars and the topological multidomain states. This feature can be used toward high storage capacity NVM.

## Declaration of competing interest

The authors declare that they have no known competing financial interests or personal relationships that could have appeared to influence the work reported in this paper.

# References

[1] Kim M, Lee K, Kim S, Lee J-H, Park B-G, Kwon D. Double-gated ferroelectric-gate field-effect-transistor for processing in memory. IEEE Electron Device Lett 2021;42(11):1607–10. http://dx.doi.org/10.1109/LED.2021.3116797.

[2] Ni K, Smith J, Ye H, Grisafe B, Rayner GB, Kummel A, et al. A novel ferroelectric superlattice based multi-level cell non-volatile memory. In: 2019 IEEE international electron devices meeting. 2019, p. 28.8.1–4. http://dx.doi.org/10.1109/IEDM19573.2019.8993670.

[3] Xu R, Liu S, Saremi S, Gao R, Wang JJ, Hong Z, et al. Kinetic control of tunable multi-state switching in ferroelectric thin films. Nature Commun 2019;10(1):1282. http://dx.doi.org/10.1038/s41467-019-09207-9.

[4] Martelli PW, Mefire SM, Luk'Yanchuk IA. Multidomain switching in the ferroelectric nanodots. Europhys Lett 2015;111(5):50001, 10.1209/0295-5075/111/50001.

[5] Lenarczyk P, Luisier M. Physical modeling of ferroelectric field-effect transistors in the negative capacitance regime. In: 2016 IEEE international conference on simulation of semiconductor processes and devices. 2016, p. 311–4. http://dx.doi.org/10.1109/SISPAD.2016.7605209.

[6] Castillo P, Cockburn B, Perugia I, Schötzau D. An A priori error analysis of the local discontinuous Galerkin method for elliptic problems. SIAM J Numer Anal 2000;38(5):1676–706. http://dx.doi.org/10.1137/S0036142900371003.

[7] Saha AK, Gupta SK. Multi-domain negative capacitance effects in metal-ferroelectric-insulator-semiconductor/metal stacks: A phase-field simulation based study. Sci Rep 2020;10(1):1–12. http://dx.doi.org/10.1038/s41598-020-66313-1.

[8] Kennedy CA, Carpenter MH. Diagonally implicit Runge–Kutta methods for stiff ODEs. Appl Numer Math 2019;146:221–44.

[9] Saha AK, Si M, Ni K, Datta S, Ye PD, Gupta SK. Ferroelectric thickness dependent domain interactions in FEFETs for memory and logic: A phase-field model based analysis. In: 2020 IEEE international electron devices meeting. 2020, p. 4.3.1–4. http://dx.doi.org/10.1109/IEDM13553.2020.9372099.

[10] Kobayashi M, Ueyama N, Jang K, Hiramoto T. Experimental study on polarization-limited operation speed of negative capacitance FET with ferroelectric HfO2. In: 2016 IEEE international electron devices meeting. 2016, p. 12.3.1–4. http://dx.doi.org/10.1109/IEDM.2016.7838402.